

Direct observations of mechanical strain-induced wavevector switching in a (Fe,Ni,Pd)₃P magnet with anisotropic Dzyaloshinskii-Moriya interaction

Shunsuke Mori¹⁺, Seiichiro Ii², Taku Moronaga³, Toru Hara², Kosuke Karube¹,
Yasujiro Taguchi¹, Yoshinori Tokura^{1,4,5}, Xiuzhen Yu¹

¹ RIKEN Center for Emergent Matter Science (CEMS), Wako, Saitama 351-0198, Japan

² Research Center for Structural Materials, National Institute for Materials Science (NIMS),
Tsukuba, Ibaraki 305-0047, Japan

³ Research Network and Facility Services Division, National Institute for Materials Science
(NIMS), Tsukuba, Ibaraki 305-0047, Japan

⁴ Department of Applied Physics, The University of Tokyo, Tokyo 113-8656, Japan.

⁵ Tokyo College, The University of Tokyo, Tokyo 113-8656, Japan.

+astamuse Co., Ltd., Tokyo 101-0054, Japan

KEYWORDS; Dzyaloshinskii–Moriya interaction, Lorentz transmission electron microscopy, Wavevector switching, Uniaxial strain, In-situ nanoindentation

ABSTRACT;

A strain-induced phase transition is one of the noteworthy phenomena in materials science and condensed matter physics. Electrical and optical switching via strain-induced phase transitions at room temperature is applicable to straintronics, which is an emerging field focusing on low energy operation of next-generation computing and memory device. While strain-induced structural and magnetic transitions have been extensively investigated, a real-space observation of these phase transitions is still a considerable challenge. In this study, we investigated magnetic textures under uniaxial compressive strain by using the Lorentz transmission electron microscopy (L-TEM) for a $(\text{Fe}_{0.63}\text{Ni}_{0.3}\text{Pd}_{0.07})_3\text{P}$ magnet with S_4 symmetry, and hence with anisotropic Dzyaloshinskii-Moriya interaction. The L-TEM observations, in conjunction with the in-situ nanoindentation technique, demonstrated a switching of the wavevector (q) of magnetic stripe domains when the strain direction is along stripes, while the q direction don't change when the strain is applied perpendicularly to the stripes. These observations are in accordance with those predicted in micromagnetic simulations. Moreover, calculations using finite element method reveal that the spatially concentrated compressive stress triggers the switching of magnetic stripes. These results provide a possibility to control the magnetic textures by application of strain in electrical materials.

Introduction

Strain-induced structural phase transitions have been widely studied in various systems such as superplastic and shape memory alloys,^{1,2} chalcogenide semiconductors,³⁻¹⁰ two-dimensional ferroelectric materials,¹¹⁻¹⁶ semiconductive or magnetic phosphide,^{17,18} with an anticipation of applications for low power consumption devices. Notably, Hou *et al.* demonstrated that MoTe₂ films exhibit a transistor-like behavior accompanied by strain-induced structural transitions,³ which is referred to as straintronics. Moreover, in chalcogenides such as MnTe and SmTe, nonvolatile memory characteristics have been demonstrated in terms of polymorphic and valence transition of the crystal structure,⁵⁻¹⁰ which are induced by thermal strain. However, the practical application of these phase transitions is still limited due to incomplete cyclic endurance attributed to low resistance to environmental factors such as heating and oxidation process.⁵

On the other hand, magnetic materials such as hexaferrite,¹⁹⁻²¹ in which magnetic properties can be modulated by lattice strain, are stable even under extreme conditions. Moreover, strain-induced modulations of the magnetic order without structural transitions gain a significant interest in the magnetism.²²⁻²⁴ Typical examples of magnetic textures are helical or conical structure, skyrmions, and ferromagnetic domains. The modulations of these textures under strain have been widely studied using neutron scattering, transport measurement, and theoretical simulations.²⁵⁻²⁷ Notably, one of the promising approach for studying these phenomena is a direct imaging of magnetic domains using in-situ Lorentz transmission electron microscopy (L-TEM), which enables us to visualize magnetic textures in nanometer scale.²⁸⁻³² To date, Shibata *et al.* has successfully observed the elongation of the individual skyrmions as well as the distorted skyrmion lattice under strain induced by cooling FeGe thin plates, which are fixed on the Si membrane, down to lower temperatures below its transition temperature of helical state (~ 280 K).³³ Their studies verified that

strain as small as 0.3% is enough to significantly deform skyrmions, as increasing the ellipticity more than 20 %. This pronounced modulation of spin textures was attributed to strain-modified anisotropic Dzyaloshinskii–Moriya interactions (DMI). However, in terms of practical applications for electrical devices, strain control of magnetic state at room temperature (RT) is more desirable. One of recent research demonstrated the real-space observations of strain-induced reversible motion of skyrmions at a RT temperature.³⁴ However, samples are locally compressed in their approach, leading to inhomogeneous strain distribution.

In this study, we focus on the strain effects upon the magnetic textures of $(\text{Fe}_{0.63}\text{Ni}_{0.3}\text{Pd}_{0.07})_3\text{P}$ (FNPP) with S_4 crystal symmetry, which is one of the magnets with anisotropic Dzyaloshinskii–Moriya interaction showing transition temperature beyond RT.^{35,36} The FNPP (001)-thin-plate, with a thickness of approximately 150 nm, hosts the magnetic stripe domain structure at RT and zero magnetic field. These stripe domains are entirely observed in as-fabricated FNPP thin plates. To investigate the effect of mechanical strain on the stripe domain structures, in-situ straining is one of promising techniques in the electron microscopy.^{34,37-40} Thus, we fabricated patterned FNPP thin plates by focused ion beam (FIB) and combined the in-situ nanoindentation measurements with L-TEM observations, to investigate the effects of uniaxial strain on the magnetic state. The captured images are analyzed in conjunction with micromagnetic simulations. The results have directly demonstrated magnetic textures and their changes under uniaxial strain at RT.

Results and Discussion

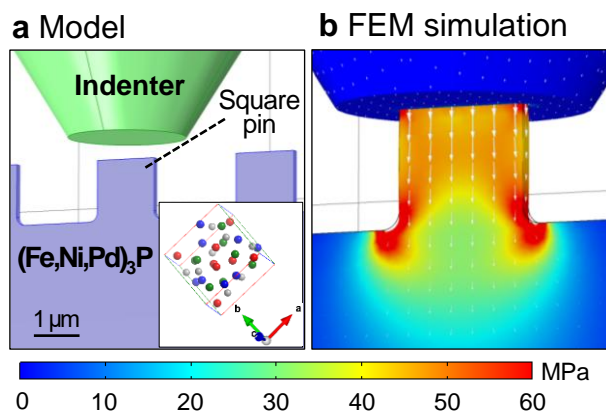


Figure 1. Schematics and finite element method (FEM) regarding a prepared setup. **a** The model of prepared $(\text{Fe}_{0.63}\text{Ni}_{0.3}\text{Pd}_{0.07})_3\text{P}$ samples and **b** expected stress and strain mapping through FEM simulation.

Preparation of the FNPP thin plate for observations. In this study, FNPP single crystals were synthesized using the self-flux method. As shown in Figure S1,S2 and Table S1,S2 in the Supplementary Information (SI), the chemical composition and structural parameters were analyzed through energy dispersive X-ray spectrometer (EDX) equipped with a scanning electron microscope (SEM) and X-ray diffraction, indicating that single-phase FNPP close to stoichiometric composition was obtained. Hence, we fabricated a square-patterned FNPP thin plate to induce uniaxial strain. Figure 1 presents the schematic overview of the experimental setup to observe the strain-induced magnetic transition in the FNPP (001) thin plate. As illustrated in Figure 1a, the top surface of FNPP thin plate was patterned with square pins, and the inset depicts a schematic image of the FNPP crystal structure viewed along the [001] axis. The dimensions of the square pins ($1.4 \mu\text{m} \times 1.4 \mu\text{m} \times 0.15 \mu\text{m}$) were designed to be smaller than the diameter ($2.7 \mu\text{m}$) of the cone-shaped indenter to apply uniaxial compressive strain. Based on this design, as depicted in Fig. 1b, the expected displacement and stress distribution within a square pin under compression were simulated through a finite element method (FEM) by using a commercial software COMSOL.⁴¹ The reported mechanical parameters for Fe_3P were employed for the simulation.⁴²

The color scale represents the stress distribution when -1% compressive strain is applied to the square pin by the indenter. The setup and mechanical parameters of simulations are described in Figure S3 in the SI. The white arrows in Figure 1b, which indicate a direction of displacement, are uniformly aligned along the indentation axis, ensuring that the current setup is possible to generate uniaxial compressive stress within the square pins. Meanwhile, the stress mapping image reveals an inhomogeneous distribution, indicating compressive stress is concentrated at the corner of square. This stress inhomogeneity plausibly arises from the boundary conditions of the sample as the edges of FNPP thin plate are fixed while compressive stress outside the square region is almost negligible as expected. Meanwhile, the grain size under surface compression on physical properties has been reported.⁴³ However, single crystal FNPP in this study is free from such an effect from grain boundaries.

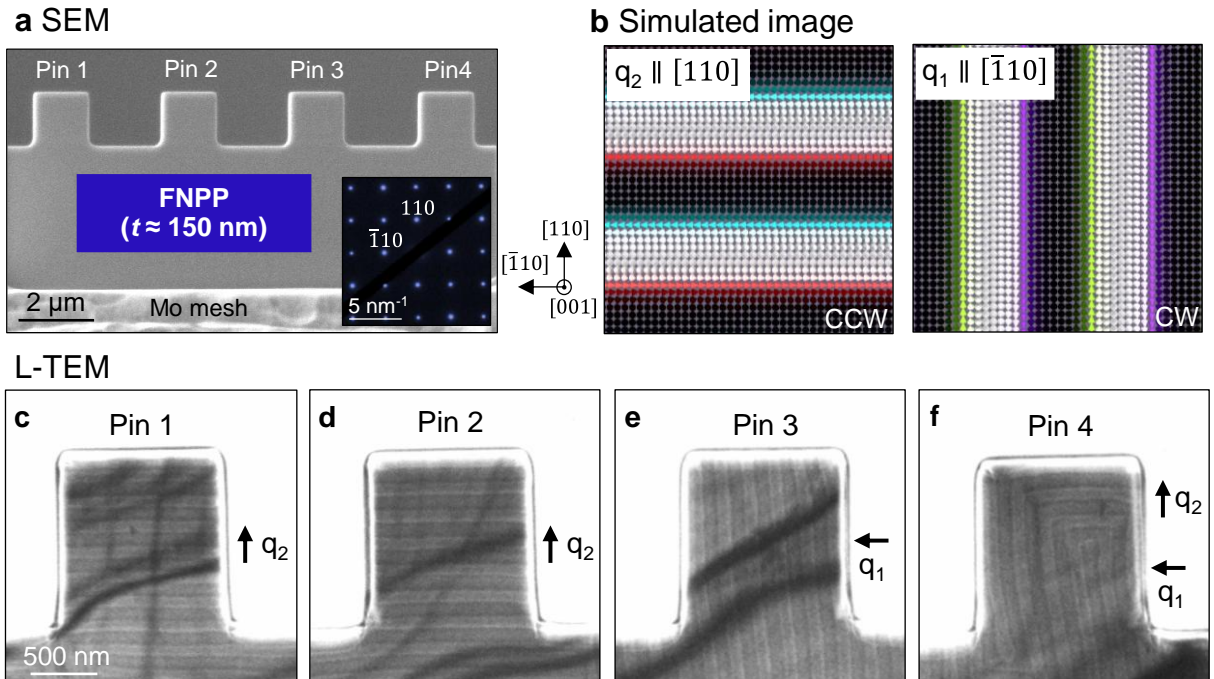


Figure 2. Microscopic images and magnetic textures of prepared FNPP with square pins. **a** The scanning electron microscopy image of the as-fabricated 4 square pins. The right inset shows the corresponding electron diffraction pattern and crystallographic indices. **b** Magnetic stripes of FNPP displayed through micromagnetic simulations. **c-f** Observed images of magnetic stripes of each pin through L-TEM observations.

Figure 2 presents the fabricated FNPP thin plate with the square pins and corresponding images of magnetic textures within each pin. As shown in the cross-sectional scanning electron microscopy (SEM) image in Figure 2a, four squares, labeled as pins 1, 2, 3, and 4, were patterned at the top surface of a 150-nm-thick FNPP thin plate. The inset displays a selected area electron diffraction (SAED) pattern along the $[001]$ axis, confirming that the crystallographic axes ($[110]$ and $[\bar{1}10]$) are successfully aligned to the sides of squares. Figure 2b presents the simulated magnetic stripes of FNPP at room temperature and zero magnetic field, indicating that these crystallographic axes correspond to two distinct directions of wavevectors, q_1 and q_2 . The magnetic stripes oriented along the $[\bar{1}10]$ and $[110]$ axes exhibit different helicities, which are clockwise (CW) for q_1 and counterclockwise (CCW) for q_2 , respectively. These magnetic textures and helicities are attributed to anisotropic DMI vectors, well consistent with the previous study.⁴⁴ The L-TEM images in Figures 2 c-f present initial magnetic textures of each square pin. The pins 1 and 2 exhibit magnetic stripes aligned with the q_2 direction while the pin 3 exhibits stripes aligned along q_1 direction. The pin 4 exhibits the mixed configuration of stripes, containing both q_1 and q_2 domains. Such designed samples enable us to systematically investigate the modulation of magnetic stripes aligned parallel and perpendicular to the applied strain. The detailed experimental procedures to fabricate these square pins with different stripe domains are described in Figure S4 in the SI.

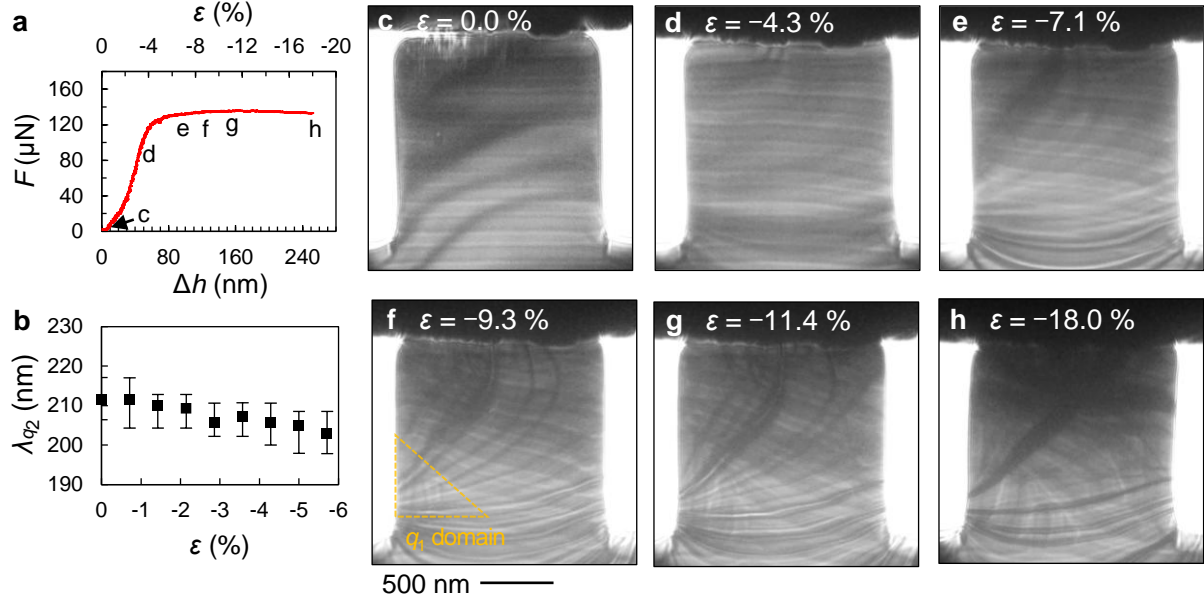


Figure 3. The results of nanoindentation test and in-situ L-TEM observations of the pin 2. **a** The measured force (F) – displacement (Δh) curve during indentation. The upper horizontal axis presents corresponding uniaxial compressive strain. **b** The strain dependence of the period of magnetic stripes. **c-h** The L-TEM images under uniaxial compressive strain ($\epsilon = -0.0, -4.3, -7.1, -9.3, -11.4, -18.0\%$).

In-situ LTEM observations under uniaxial compression. First, we focus on the magnetic stripes with the q_2 in the pins 1 and 2, where the q is aligned parallel to the direction of compressive strain. Figure 3a presents the force (F) versus the displacement (Δh) of the top surface from the initial position for the pin 2, obtained through the in-situ nanoindentation test. The compressive strain, which is also displayed on the upper horizontal axis, is simply estimated ($\epsilon = -\Delta h/h_0$) based on the initial height of samples (h_0) as schematically illustrated in Figure S5a in the SI. This $F - \Delta h$ curve exhibits a linear relationship during the elastic deformation (up to approximately -4%). On the other hand, the F becomes saturated at larger compressive strain more than -4% , indicating that the plastic deformation proceeds in this region. The $F - \Delta h$ curve terminates as the pin 2 is finally fractured when the compressive strain exceeds -18.0% . The maximum strain varies slightly between different pins, which is likely due to slight changes in sample thickness and indentation conditions (see detail discussions in the SI). Figure 3b and 3c-f present the strain dependence of the period of magnetic stripes and a series of L-TEM images during compressive process ($\epsilon = -0.0,$

-4.3, -7.1, -9.3, -11.4, -18.0 %). The stripe period decreases with increasing compressive strain during elastic region, implying the possible enhancement of DMI strength and fluctuations of modulated magnetic stripes with the q_2 domain. At the end of the elastic region (Figure 3d), the bending of the magnetic strip is evident. This bending of the magnetic stripe becomes more pronounced during the plastic deformation (Fig. 3e). Notably, Δh exceeds the thickness of square pins during plastic deformation, indicating dislocations activate during nanoindentation. Xiang et al. demonstrated that a high concentration of dislocations induces the rotation of magnetic moments,⁴⁵ suggesting that structural defects in FNPP likely contribute to the bending of the magnetic stripe in this study. According to a previous study, it is hard to observe distinctive motions of magnetic stripes.³⁴ In contrast, we succeeded in clearly observing strain-induced motion of magnetic stripes under the current setup by applying uniaxial compressive strain. Moreover, this bent stripe was observed to transform into the vertical stripes with the q_1 , as enclosed by an orange triangle in Fig. 3f. The q_1 domain exhibits an evolution with an increase of strain ($\varepsilon = -11.4, -18.0$ %), indicating that the wavevector aligned parallel to the direction of strain is unstable under uniaxial compression. The growth of the q_1 domain starts from the left-bottom corner of the square, consistent with FEM simulations (Figure 1b), which reveals that the compressive stress concentrates at the bottom corners of the square. These results suggest that the conversion of helical stripes was triggered by the concentration of compressive stress at the corner. The observed behavior is reproducible according to the results for the pin 1 in Figure S5b-g in the SI. The $F - \Delta h$ curve for the pin 1 includes both loading and unloading process after reaching a maximum strain of -14.3 %, as the pin 1 is not fractured during the indentation test. The displacement at the end of unloading is approximately 20 nm, which is plausible due to residual strain ($\varepsilon = -1.4$ %) as a plastic deformation. During the loading process, the magnetic stripes with

the q_2 exhibits bending and transformation into the q_1 domain. The transformation of the stripes with the q_2 to q_1 in pin 1 initiates from the right-bottom corner of the square, which is in accordance with the stress concentration in Figure 1b. The L-TEM image after unloading is also captured as shown in Figure S5g in the SI, indicating that the q_1 domain becomes non-volatile and stable owing to residual compressive strain. The results observed in the pins 1 and 2 are shown in Movie S1 and S2.

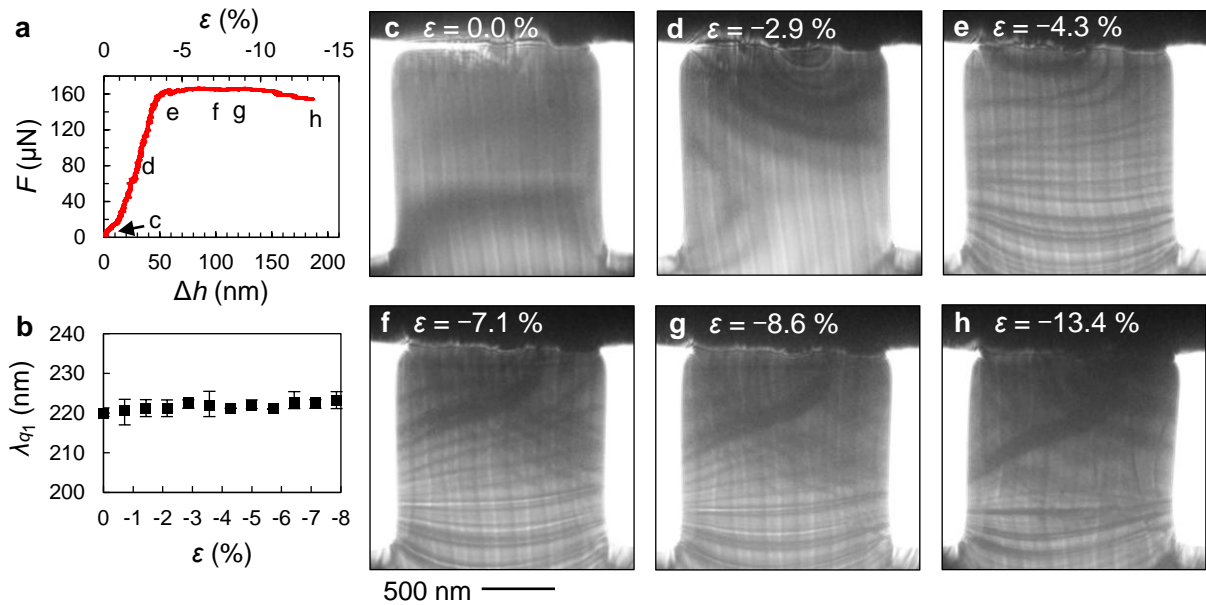


Figure 4. The results of the nanoindentation test and in-situ L-TEM observations of the pin 3. **a** The measured F – Δh curve during indentation. The upper horizontal axis presents corresponding uniaxial compressive strain. **b** The strain dependence of the period of magnetic stripes. **c–h** The L-TEM image series under uniaxial compressive strain ($\epsilon = -0.0, -2.9, -4.3, -7.1, -8.6, -13.4$ %).

To investigate the strain effect on the q vectors, we focus on the magnetic stripe with the q_1 within the pin 3 as shown in Figure 4. According to the $F - \Delta h$ curve in Figure 4a, the elastic deformation occurs consistently at smaller compressive strain up to approximately -4%. In contrast to the observations in Fig. 3, the helical period and L-TEM images in Figures 4b-e exhibit negligible changes; e.g., the bending of magnetic stripes is not prominent in this series of L-TEM images.

Even during the plastic deformation ($\varepsilon = -7.1, -8.6, -13.4 \%$), the L-TEM images in Figures 4f-h exhibit no distinctive bending or transformation of the stripes. The distinct behavior indicates that the wavevector normal to the uniaxial compressive strain is robust. Furthermore, the stability of the q_1 domain is reproducibly confirmed by the L-TEM observations for the pin 4, which hosts both q_2 and q_1 domains, as shown in Figure S6 in the SI. The q_1 domain, which is observed at the bottom of the square, exhibits negligible changes even under stress concentration. Meanwhile, the slight tilting of the q_1 domain is observed in both pins 3 and 4. This tilting is plausible because the indenter does not compress the sample perfectly along the vertical direction due to roughness and alignment of the top of the indenter. The FEM simulations have been carried out as shown in Figure S7 in the SI, to present the expected stress distribution when the indenter and pins are not perfectly parallel each other during compression. In such scenarios, the direction of compressive strain slightly deviates from the symmetry axis of the pin, resulting in a minor realignment of the magnetic stripes. Moreover, the asymmetry in the stress distribution is a possible reason to explain the fractures observed in some pins. The experimental evidence observed in the pins 3 and 4 are shown in Movie S3 and S4.

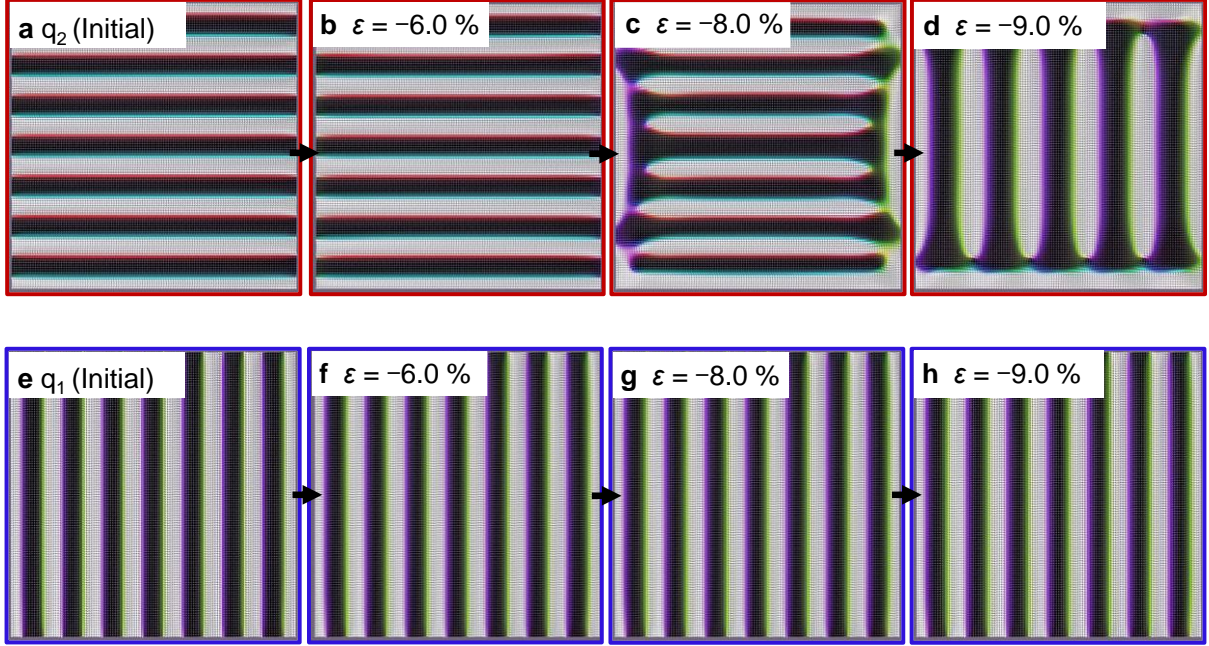


Figure 5. Simulated magnetic stripes under uniaxial compressive strain. **a-d** The image series of magnetic stripes when q is parallel to the strain. **e-h** The image series of magnetic stripes when q is perpendicular to the strain. Both series of magnetic textures are simulated at the compressive strain of 0.0, -6.0, -8.0, and -9.0%.

Micromagnetic simulations. To theoretically investigate the magnetic stripe under compressive strain, we carried out micromagnetic simulations,⁴⁶ visualizing the dynamics of both q_2 and q_1 domains of FNPP. Magnetoelastic coupling constants ($B_1 = 2.0 \times 10^5$) of the sample are tentatively adopted in this study to consider the effect of strain on the magnetic system, namely, a magnetoelastic field.⁴⁷ In this calculation with the positive B_1 , compressive strain along y-axis enhances the magnetoelastic field along the $[110]$ direction, which is added to the effective magnetic field. The details of material parameters for simulations are shown in the Method section.^{44,48,49} Figure 5 presents the simulated magnetic stripes with an increase in uniaxial compressive strain along the longitudinal direction. First, Figure 5 a-d represents a transition behavior of the q_2 domain. The magnetic stripe with the q_2 domain shows slight bending at the edge of square and transition to the q_1 domain ($\varepsilon = -6.0, -8.0\%$). Finally, the magnetic stripe in the square entirely transforms into the q_1 domain ($\varepsilon = -9.0\%$). Similarly, the 90° rotation of magnetic stripes occurs at the square corner, as shown in Fig. 3f-h. These results reveal that the wavevector

perpendicular to the strain is stable, supporting the observed results in the pin 2. On the other hand, Figure 5 e-h indicates that the change of q_1 domain with varying the stress is almost negligible, which is in accordance with the observed results in the pin 3 in Fig. 4. These simulations comply with observations, suggesting that the magnetoelastic effect is key factor to stabilize the magnetic stripe domains with q along a perpendicular direction to the strain. Recently, similar behaviors have been observed in a ferromagnetic Ni thin plate.⁵⁰ The direction of magnetic stripes of Ni is also ordered along uniaxial strain, in agreement with micromagnetic simulations by adding the magnetoelastic interaction. These results demonstrate that the uniaxial strain and magnetoelasticity systematically enable us to control wavevectors of magnetic textures. These behaviors depend on the magnetoelastic coupling constants and strain dependence of physical parameters.⁵¹⁻⁵⁴ In this study, the strain dependence of magnetic stripe periods in Fig. 3b suggests either an increase in the DMI constant or a decrease in exchange stiffness. Moreover, these physical parameters can be modulated by designing composite materials.⁵⁵ The detailed investigations of physical properties and varying material parameters under strain are the scope of the future study.

Conclusions

In summary, we successfully performed the in-situ observations of magnetic stripes under uniaxial compressive strain in the FIB-fabricated FNPP plates by the nanoindentation technique. The magnetic stripes with the wavevector parallel to the strain direction have been bent and then transformed into the stripes with wavevector perpendicular to the stress direction by applying the compressive stress, in contrast to the case of magnetic stripes with the wavevector normal to the strain in the FNPP thin plate. The micromagnetic simulations reveal the wavevector switching

under compressive strain. The observed phenomena are likely to be driven by stress concentration at the corner of square pins, which is in accordance with FEM simulations. These systematic investigations of the magnetic textures under uniaxial compressive strain provide important insights to control the strain-induced magnetic transition in electrical devices. This study highlights a promising pathway for the application of magnetic materials in straintronics field.

Methods

Sample preparation. High-quality bulk single crystals of $(\text{Fe}_{0.63}\text{Ni}_{0.3}\text{Pd}_{0.07})_3\text{P}$ are required for the fabrication of microdevices. Standard techniques by annealing stoichiometric powders below the melting point or electrodeposition, for example as described in other studies,^{56,57} do not yield large single crystals. Therefore, we used a self-flux method, as described in the previous study,³⁶ in which starting materials with metal-rich non-stoichiometric ratio of Fe : Ni : Pd : P = 1.8 : 1.1 : 0.6 : 1 were sealed in an evacuated quartz tube and slowly cooled from 970°C to 910°C.

In general, cation-anion stoichiometry of metal-metalloid compounds significantly affects their chemical and physical properties.⁵⁸ To clarify the chemical composition of the obtained FNPP, the SEM-EDX was employed. The results show the chemical composition of the present sample is $\text{Fe}_{1.897(7)}\text{Ni}_{0.892(8)}\text{Pd}_{0.217(3)}\text{P}_{0.994(5)}$, very close to the stoichiometric composition: $(\text{Fe}_{0.63}\text{Ni}_{0.30}\text{Pd}_{0.07})_3\text{P}$. Moreover, determining the occupation of crystallographic positions is important for compounds.⁵⁹ The tetragonal crystal structure of single-phase M_3P (space group $I\bar{4}$) was confirmed by powder X-ray diffraction with Cu $K\alpha$ radiation and the Rietveld analysis using RIETAN-FP program.⁶⁰ According to the SEM-EDX and X-ray diffraction, it is clear that the single crystal used in the present L-TEM experiment is the single-phase stoichiometric FNPP.

The (001) thin plate of FNPP was fabricated and thinned (thickness of approximately 150 nm) through the FIB technique (Helios 5UX, FEI). The obtained thin plate was picked up and put at the top of Mo mesh. To precisely apply the uniaxial compressive strain, Mo mesh was also milled and flattened in advance. After fixing the FNPP thin plate on the flattened Mo mesh, four square pins with dimensions of $1.4\ \mu\text{m} \times 1.4\ \mu\text{m} \times 0.15\ \mu\text{m}$ were patterned at the top surface by FIB. Eventually, both sides of squared pins are cleaned by low energy ion beam.

TEM observations. Real-space observations of magnetic textures under mechanical strain were performed by transmission electron microscopes (JEM-2800, JEOL) equipped with a nanoindentation holder (PI95, Bruker Co.). A truncated cone shape indenter was employed, and the maximum displacement was 1000 nm. The tip was indented at the loading rates of 1 nm /s. The uniaxial compressive strain during the indentation test was simply estimated from the distance and initial height of sample, which is described in Figure S2. The static image and movie of magnetic textures were simultaneously captured by in-situ L-TEM observation at room temperature and zero magnetic field. These LTEM images of a magnetic texture are acquired at the under-defocus mode.

FEM simulations. The simulation of stress distribution was conducted by finite element method (FEM) using COMSOL Multiphysics software. Figure S1a and S1b present the model and geometry of FEM simulations. The edges of the deformed square pin compressed by an indenter are defined as free planes while other edges are considered as constraint planes. Stress mapping is calculated by directly compressing the square pin, where the modulus of the mother compound, Fe_3P , is tentatively used for the mechanical properties of FNPP. The mechanical properties of the indenter are configured using standard parameters for diamond.

Micromagnetic simulation. We carried out micromagnetic simulations based on the Landau-Lifshitz-Gilbert (LLG) equation using the MuMax3 software.⁴⁵ For the simulations of q-vector switching, the size of the magnet was $L_x \times L_y = 1400 \times 1400 \text{ nm}^2$, and we set open boundary conditions. The x and y axes correspond to the experimental $[110]$ and $[\bar{1}10]$ crystal axes, respectively, with a righthanded helix stabilized in x-direction and a lefthanded helix in the y-direction. The material parameters were chosen according to the previous study at $T = 300 \text{ K}$: saturated magnetization $M_s = 4.17 \times 10^5 \text{ A m}^{-1}$; exchange stiffness $A = 8.1 \times 10^{-12} \text{ J m}^{-1}$, and uniaxial anisotropy constant $K_u = 3.1 \times 10^4 \text{ J m}^{-3}$ along the z axis. The Gilbert damping constant was set to $\alpha = 0.03$. In this study, anisotropic DMI constant was set to $D = 4.0 \times 10^{-4} \text{ J m}^{-2}$. To achieve anisotropic DMI, we added custom energy density and effective field terms using the MuMax3 built-in functions. The field term is defined as $\mathbf{B} = 2D_{ani}(\partial_y n_z \hat{x} + \partial_x n_z \hat{y} - (\partial_x n_y + \partial_y n_x) \hat{z})$, where n_i is the i th component of the magnetization, and the energy density expression is defined as $E_D = -\frac{1}{2} \mathbf{n} \cdot \mathbf{B}$. To take the strain effect into consideration, we tentatively employed magnetoelastic coupling constant $B_1 = 2.0 \times 10^5$. Based on these parameters, magnetic stripes are simulated under different vertical compressive strain e_{yy} between 0 and -9%. In this study, these parameters of FNPP were tentatively considered as constants.

ASSOCIATED CONTENT

Supporting Information

The Supporting Information is available.

The composition analysis of fabricated FNPP, The structural analysis of fabricated FNPP, Finite element simulations (FEM) of FNPP thin plate, Fabrication procedures of square pins, Schematics

and representations of nanoindentation tests with a series of L-TEM image for pin 1, Nanoindentation and a series of L-TEM image for pin 4, FEM simulation of deviation from uniaxial strain

AUTHOR INFORMATION

Corresponding Author

Shunsuke Mori; shunsuke.mori.fs@a.riken.jp and Xiuzhen Yu; yu_x@riken.jp

Present Addresses

¹Shunsuke Mori; s.mori@astamuse.co.jp

Author Contributions

The manuscript was written through contributions of all authors. All authors have given approval to the final version of the manuscript.

Funding Sources

This work was supported in part by Grants-In-Aid for Scientific Research (A) (Grant No. 19H00660), Research Activity Start-up (Grant No. 22K20363), and Early-Career Scientists (23K13639), Grants-In-Aid for Scientific Research (B) (Grant No. 23K26534), Grants-In-Aid for Scientific Research (C) (Grant No. 23K04365), Grants-In-Aid for Scientific Research (A) (Grant No. 24H00389) from the Japan Society for the Promotion of Science (JSPS) and the Japan Science and Technology Agency (JST) CREST program (Grant No. JPMJCR20T1), Japan.

ACKNOWLEDGMENT

The authors thank Dr. Fehmi Yasin, Dr. Yao Guang, Dr. Yi Ling Chiew, and Ms. Kiyomi Nakajima for their experimental supports and discussions; Prof. Yoshifumi Oshima for the fruitful discussions about in-situ straining.

REFERENCES

1. Otsuka, K.; Shimizu, K. Pseudoelasticity and Shape Memory Effects in Alloys. *Int. Met. Rev.* **1986**, *31*, 93–114. <https://doi.org/10.1179/imtr.1986.31.1.93>
2. Otsuka, K.; Wayman, C. M., Shape Memory Materials. Cambridge University Press, (1999). isbn: 9780521663847
3. Hou, W.; Azizimanesh, A.; Sewaket, A.; Peña, T.; Watson, C.; Liu, M.; Askari, H.; Wu, S. M. Strain-Based Room-Temperature Non-Volatile MoTe₂ Ferroelectric Phase Change Transistor. *Nat. Nanotechnol.* **2019**, *14*, 713–718. <https://doi.org/10.1038/s41565-019-0466-2>
4. Awate, S. S.; Xu, K.; Liang, J.; Katz, B.; Muzzio, R.; Crespi, V. H.; Katoch, J.; Fullerton, S. K. Strain-Induced 2H to 1T' Phase Transition in Suspended MoTe₂ Using Electric Double Layer Gating. *ACS Nano* **2023**, *17*, 22388–22398. <https://doi.org/10.1021/acsnano.3c04701>
5. Mori, S.; Hatayama, S.; Shuang, Y.; Ando, D.; Sutou, Y. Reversible Displacive Transformation in MnTe Polymorphic Semiconductor. *Nat. Commun.* **2020**, *11*, 85. <https://doi.org/10.1038/s41467-019-13747-5>
6. Mori, S.; Ando, D.; Sutou, Y. Sequential Two-Stage Displacive Transformation from β to α via β' Phase in Polymorphic MnTe Film. *Mater. Des.* **2020**, *196*, 109141. <https://doi.org/10.1016/j.matdes.2020.109141>
7. Mori, S.; Wang, Y.; Ando, D.; Narita, F.; Sutou, Y. Thermal Stress Control of the Polymorphic Transformation in MnTe Semiconductor Films. *Materialia* **2022**, *24*, 101493. <https://doi.org/10.1016/j.mtla.2022.101493>
8. Mori, S.; Tanimura, H.; Ichitsubo, T.; Sutou, Y. Photoinduced Nonvolatile Displacive Transformation and Optical Switching in MnTe Semiconductors. *ACS Appl. Mater. Interfaces* **2023**, *15*, 42730–42736. <https://doi.org/10.1021/acсами.3c07537>
9. Mori, S.; Sutou, Y. Polymorphic Transformation from Metastable β to Stable α Phase in MnTe Flake. *Jpn. J. Appl. Phys.* **2024**, *63*, 045502. <https://doi.org/10.35848/1347-4065/ad32e7>
10. Hatayama, S.; Mori, S.; Saito, Y.; Fons, P. J.; Shuang, Y.; Sutou, Y. Nonvolatile Isomorphic Valence Transition in SmTe Films. *ACS Nano* **2024**, *18*, 2972–2981. <https://doi.org/10.1021/acsnano.3c07960>
11. Zhao, J. Z.; Chen, L. C.; Xu, B.; Zheng, B. B.; Fan, J.; Xu, H. Strain-Tunable Out-of-Plane Polarization in Two-Dimensional Materials. *Phys. Rev. B* **2020**, *101* (12), 121407. <https://doi.org/10.1103/PhysRevB.101.121407>
12. Orlova, N. N.; Timonina, A. V.; Kolesnikov, N. N.; Deviatov, E. V. Switching Ferroelectricity

- in SnSe across Phase Transition. *EPL (Europhysics Letters)* **2021**, *135*, 37002. <https://doi.org/10.1209/0295-5075/ac2247>
13. Gong, Z.; Liu, J. Z.; Ding, X.; Sun, J.; Deng, J. Strain-Aided Room-Temperature Second-Order Ferroelectric Phase Transition in Monolayer PbTe: Deep Potential Molecular Dynamics Simulations. *Phys. Rev. B* **2023**, *108*, 134112. <https://doi.org/10.1103/PhysRevB.108.134112>
 14. Shi, C.; Mao, N.; Zhang, K.; Zhang, T.; Chiu, M.-H.; Ashen, K.; Wang, B.; Tang, X.; Guo, G.; Lei, S.; Chen, L.; Cao, Y.; Qian, X.; Kong, J.; Han, Y. Domain-Dependent Strain and Stacking in Two-Dimensional van der Waals Ferroelectrics. *Nat. Commun.* **2023**, *14*, 7168. <https://doi.org/10.1038/s41467-023-42947-3>
 15. Gong, Z.; Liu, J. Z.; Ding, X.; Sun, J.; Deng, J. Strain-Induced Two-Dimensional Relaxor Ferroelectrics in Se-Doped PbTe. *Phys. Rev. B* **2024**, *109*, 054117. <https://doi.org/10.1103/PhysRevB.109.054117>
 16. Ding, Y.; Huang, A.; Wu, Y.; Zhou, L. Strain-induced ferroelectric phase transition and second-harmonic generation enhancement in NbOCl₂ monolayer. *Appl. Phys. Lett.* **2024**, *125*, 151902. <https://doi.org/10.1063/5.0235837>
 17. Lin, C.-M.; Lin, S.-C.; Tseng, Y.-C.; Huang, T.; Kung, H.-H.; Chuang, Y.-C.; Liao, Y.-F.; Wu, B.-R.; Jian, S.-R.; Juang, J.-Y. Tuning the Onset Pressure of Pressure-Induced Phase Transition in Indium Phosphide by Extrinsic Doping. *J. Phys. Chem. Solids* **2022**, *161*, 110487. <https://doi.org/10.1016/j.jpcs.2021.110487>
 18. Panasyuk, M. I.; Zubar, T. I.; Usovich, T. I.; Tishkevich, D. I.; Kanafyev, O. D.; Fedkin, V. A.; Kotelnikova, A. N.; Trukhanov, S. V.; Michels, D.; Lyakhov, D.; Vershinina, T. N.; Fedosyuk, V. M.; Trukhanov, A. V. Mechanism of Bubbles Formation and Anomalous Phase Separation in the CoNiP System. *Sci. Rep.* **2023**, *13*, 5829. <https://doi.org/10.1038/s41598-023-33146-7>
 19. Trukhanov, A. V.; Kostishyn, V. G.; Panina, L. V.; Jabarov, S. H.; Korovushkin, V. V.; Trukhanov, S. V.; Trukhanova, E. L. Magnetic Properties and Mössbauer Study of Gallium Doped M-Type Barium Hexaferrites. *Ceram. Int.* **2017**, *43*, 12822–12827. <https://doi.org/10.1016/j.ceramint.2017.06.172>
 20. Kumar, S.; Supriya, S.; Pandey, R.; Pradhan, L. K.; Singh, R. K.; Kar, M. Effect of Lattice Strain on Structural and Magnetic Properties of Ca Substituted Barium Hexaferrite. *J. Magn. Magn. Mater.* **2018**, *458*, 30–35. <https://doi.org/10.1016/j.jmmm.2018.02.093>
 21. Trukhanov, S. V.; Trukhanov, A. V.; Kostishyn, V. G.; Zabeivorota, N. S.; Panina, L. V.; Trukhanov, A. V.; Turchenko, V. A.; Trukhanova, E. L.; Oleynik, V. V.; Yakovenko, O. S.; Matzui, L. Y.; Zhivulin, V. E. High-Frequency Absorption Properties of Gallium Weakly Doped Barium Hexaferrites. *Philos. Mag.* **2019**, *99*, 585–605. <https://doi.org/10.1080/14786435.2018.1547431>
 22. Esteras, D. L.; Rybakov, A.; Ruiz, A. M.; Baldoví J. J. Magnon Straintronics in the 2D van der Waals Ferromagnet CrSBr from First-Principles. *Nano Lett.* **2022**, *22*, 8771–8778. <https://doi.org/10.1021/acs.nanolett.2c02863>
 23. Bandyopadhyay, S.; Atulasimha, J.; Barman, A. Magnetic Straintronics: Manipulating the Magnetization of Magnetostrictive Nanomagnets with Strain for Energy-Efficient Applications. *Appl. Phys. Rev.* **2021**, *8*, 041323. <https://doi.org/10.1063/5.0062993>
 24. Bandyopadhyay, S. Perspective: There is plenty of room for magnetic straintronics in the

- analog domain. *npj Spintronics* **2024**, 2, 18. <https://doi.org/10.1038/s44306-024-00018-3>
25. Nii, Y.; Nakajima, T.; Kikkawa, A.; Yamasaki, Y.; Ohishi, K.; Suzuki, J.; Taguchi, Y.; Arima, T.; Tokura, Y.; Iwasa, Y. Uniaxial Stress Control of Skyrmion phase. *Nat. Commun.* **2015**, 6, 8539. <https://doi.org/10.1038/ncomms9539>
 26. Kimbell, G.; Kim, C.; Wu, W.; Cuoco, M.; Robinson, J. W. A. Challenges in identifying chiral spin textures via the topological Hall effect. *Commun. Mater.* **2022**, 3, 19. <https://doi.org/10.1038/s43246-022-00238-2>
 27. Tanaka, K.; Sugawara, R.; Mochizuki, M. Theoretical Study on Stabilization and Destabilization of Magnetic Skyrmions by Uniaxial-Strain-Induced Anisotropic Dzyaloshinskii-Moriya Interactions. *Phys. Rev. Mater.* **2020**, 4, 034404. <https://doi.org/10.1103/PhysRevMaterials.4.034404>
 28. Raabe, J.; Pulwey, R.; Sattler, R.; Schweinböck, T.; Zweck, J.; Weiss, D. Magnetization Pattern of Ferromagnetic Nanodisks. *J. Appl. Phys.* **2000**, 88, 4437–4441. <https://doi.org/10.1063/1.1289216>
 29. Mori, S.; Asaka, T.; Matsui, Y. Observation of Magnetic Domain Structure in Phase-Separated Manganites by Lorentz Electron Microscopy. *J. Electron Microsc.* **2002**, 51, 225–229. <https://doi.org/10.1093/jmicro/51.4.225>
 30. Nagai, T.; Yamada, H.; Konoto, M.; Arima, T.; Kawasaki, M.; Kimoto, K.; Matsui, Y.; Tokura, Y. Direct Observation of the Spin Structures of Vortex Domain Walls in Ferromagnetic Nanowires. *Phys. Rev. B* **2008**, 78, 180414. <https://doi.org/10.1103/PhysRevB.78.180414>
 31. Yu, X. Z.; Onose, Y.; Kanazawa, N.; Park, J. H.; Han, J. H.; Matsui, Y.; Nagaosa, N.; Tokura, Y. Real-Space Observation of a Two-Dimensional Skyrmion Crystal. *Nature* **2010**, 465, 901–904. <https://doi.org/10.1038/nature09124>
 32. Budruk, A.; Pathak, C.; Petford-Long, A.; Graef, M. D. In-situ Lorentz TEM Study of Magnetic Domain Wall Mobility in Amartensitic Ni-Mn-Ga Alloy. *Microsc. Microanal.* **2011**, 17, 1858–1859. <https://doi.org/10.1017/S1431927611010166>
 33. Shibata, K.; Iwasaki, J.; Kanazawa, N.; Aizawa, S.; Tanigaki, T.; Shirai, M.; Nakajima, T.; Kubota, M.; Kawasaki, M.; Park, H. S.; Shindo, D.; Nagaosa, N.; Tokura, Y. Large Anisotropic Deformation of Skyrmions in Strained Crystal. *Nat. Nanotechnol.* **2015**, 10, 589–592 (2015). <https://doi.org/10.1038/nnano.2015.113>
 34. Liu, C.; Wang, J.; He, W.; Zhang, C.; Zhang, S.; Yuan, S.; Hou, Z.; Qin, M.; Xu, Y.; Gao, X.; Peng, Y.; Liu, K.; Qiu, Z. Q.; Liu, J.-M.; Zhang, X. Strain-Induced Reversible Motion of Skyrmions at Room Temperature, *ACS Nano* **2024**, 18, 761–769. <https://doi.org/10.1021/acsnano.3c09090>
 35. Karube, K.; Peng, L.; Masell, J.; Yu, X.; Kagawa, F.; Tokura, Y.; Taguchi, Y. Room-Temperature Antiskyrmions and Sawtooth Surface Textures in a Non-Centrosymmetric Magnet with S_4 Symmetry. *Nat. Mater.* **2021**, 20, 335–340. <https://doi.org/10.1038/s41563-020-00898-w>
 36. Karube, K.; Peng, L.; Masell, J.; Hemmida, M.; Nidda, H.-A. K.; Kézsmárki, I.; Yu, X.; Tokura, Y.; Taguchi, Y. Doping Control of Magnetic Anisotropy for Stable Antiskyrmion Formation in Schreibersite (Fe, Ni)₃P with S_4 Symmetry. *Adv. Mater.* **2022**, 34, 2108770. <https://doi.org/10.1002/adma.202108770>

37. Ii, S.; Enami, T.; Ohmura, T.; Tsurekawa, S. Direct Measurement of Shear Stress for Dislocation Transferring across $\{111\}$ $\Sigma 3$ Grain Boundary in Aluminum Bicrystal via In Situ Straining TEM. *Scripta Mater.* **2022**, *221*, 114953. <https://doi.org/10.1016/j.scriptamat.2022.114953>
38. Li, H.; Ii, S.; T. Nobuhiro; Ohmura, T. Direct Observation of Grain Boundary Formation in Bcc Iron through TEM In Situ Compression Test. *Scripta Mater.* **2022**, *207*, 114275. <https://doi.org/10.1016/j.scriptamat.2021.114275>
39. Ii, S.; Enami, T.; Ohmura, T.; Tsurekawa, S. Direct Characterization of the Relation between the Mechanical Response and Microstructure Evolution in Aluminum by Transmission Electron Microscopy In Situ Straining. *Materials* **2021**, *14*, 1431. <https://doi.org/10.3390/ma14061431>
40. Qu, H.; Yano, K. H.; H. Patki, P. V.; Swenson, M. J.; Wharry, J. P. Understanding Plasticity in Irradiated Alloys through TEM In Situ Compression Pillar Tests. *J. Mater. Res.* **2020**, *35*, 1037–1050. <https://doi.org/10.1557/jmr.2019.295>
41. COMSOL Multiphysics® v. 6.3. www.comsol.com. COMSOL AB, Stockholm, Sweden. <https://www.comsol.com/release/6.3>
42. Wu, J.; Chong, X.; Zhou, R.; Jiang, Y.; Feng J. Structure, Stability, Mechanical and Electronic Properties of Fe–P Binary Compounds by First-Principles Calculations. *RSC Adv.* **2015**, *5*, 81943–81956. <https://doi.org/10.1039/C5RA09875K>
43. Trukhanov, S. V.; Lobanovski, L. S.; Bushinsky, M. V.; Khomchenko, V. A.; Fedotova, V. V.; Troyanchuk, I. O.; Szymczak, H. Microstructure Evolution and Magnetoresistance of the A-Site Ordered Ba-Doped Manganites. *Semiconductors* **2007**, *41*, 507–511. <https://doi.org/10.1134/S1063782607050041>
44. Yasin, F. S.; Masell, J.; Karube, K.; Shindo, D.; Taguchi, Y.; Tokura, Y.; Yu, X. Heat Current-Driven Topological Spin Texture Transformations and Helical q-Vector Switching. *Nat. Commun.* **2023**, *14*, 7094. <https://doi.org/10.1038/s41467-023-42846-7>
45. Xiang, Z.; Sun, Q.; Wang, S. Effect of Dislocation Pattern on the Magnetic Domain Structure of Pure Polycrystalline Ni. *J. Mater. Res. Technol.* **2022**, *17*, 1896–1900. <https://doi.org/10.1016/j.jmrt.2022.01.107>
46. Vansteenkiste, A; Leliaert, J.; Dvornik, M.; Helsen, M.; Garcia-Sanchez, F.; Waeyenberge, B. V. The Design and Verification of MuMax3. *AIP Adv.* **2014**, *4*, 107133. <https://doi.org/10.1063/1.4899186>
47. Vanderveken, F; Mulkers, J.; Leliaert, J.; Waeyenberge, B. V.; Sorée, B.; Zografos, O.; Ciubotaru, F.; Adelman, C. Finite Difference Magnetoelastic Simulator. *Open Res. Eur.* **2021**, *1*, 35. <https://doi.org/10.12688/openreseurope.13302.1>
48. Nakamura, D.; Karube, K.; Liu, Y.; Kagawa, F.; Yu, X.; Tokura, Y.; Taguchi, Y. Observation of Resonant Spin Excitation with In-Plane Spin Wave Propagation in Hybrid Antiskyrmion Strings. *Phys. Rev. B* **2024**, *110*, 024418. <https://doi.org/10.1103/PhysRevB.110.024418>
49. Guang, Y.; Zhang X.; Liu Y.; Peng L.; Yasin, F. S.; Karube, K.; Nakamura, D.; Nagaosa, N.; Taguchi, Y.; Mochizuki, M.; Tokura, Y.; Yu, X. Confined Antiskyrmion Motion Driven by Electric Current Excitations. *Nat. Commun.* **2024**, *15*, 7701. <https://doi.org/10.1038/s41467->

50. Kong, D.; Kovács, A.; Charilaou, M.; Zheng, F.; Wang, L.; Han, X. Dunin-Borkowski, R. E. Direct Observation of Tensile-Strain-Induced Nanoscale Magnetic Hardening. *Nat. Commun.* **2023**, *14*, 3963. <https://doi.org/10.1038/s41467-023-39650-8>
51. Gusev, N. S.; Sadovnikov, A. V.; Nikitov, S. A.; Sapozhnikov, M. V.; Udalov, O. G. Manipulation of the Dzyaloshinskii–Moriya Interaction in Co/Pt Multilayers with Strain. *Phys. Rev. Lett.* **2020**, *124*, 157202. <https://doi.org/10.1103/PhysRevLett.124.157202>
52. Udalov, O. G.; Beloborodov, I. S. Strain-Dependent Dzyaloshinskii–Moriya Interaction in a Ferromagnet/Heavy-Metal Bilayer. *Phys. Rev. B* **2020**, *102*, 134422. <https://doi.org/10.1103/PhysRevB.102.134422>
53. O'Handley, R. C.; Sun, S. -W. Strained Layers and Magnetoelastic Coupling. *J. Magn. Magn. Mater.* **1992**, *104*, 1717–1720. [https://doi.org/10.1016/0304-8853\(92\)91522-U](https://doi.org/10.1016/0304-8853(92)91522-U)
54. Wedler, G.; Walz, J.; Greuer, A.; Koch, R. Stress Dependence of the Magnetoelastic Coupling Constants B_1 and B_2 of Epitaxial Fe(001). *Phys. Rev. B* **1999**, *60*, R11313. <https://doi.org/10.1103/PhysRevB.60.R11313>
55. Yakovenko, O.; Lazarenko, O.; Matzui, L.; Vovchenko, L.; Borovoy, M.; Tesel'ko, P.; Lozitsky, O.; Astapovich, K.; Trukhanov, A.; Trukhanov, S. Effect of Ga Content on Magnetic Properties of BaFe_{12-x}Ga_xO₁₉/Epoxy Composites. *J. Mater. Sci.* **2020**, *55*, 9385–9395. <https://doi.org/10.1007/s10853-020-04661-z>
56. Troyanchuk, I. O.; Trukhanov, S. V.; Shapovalova, E. F.; Khomchenko, V. A.; Tovar, M.; Szymczak, H. The Influence of Oxygen Vacancies on the Magnetic State of La_{0.50}D_{0.50}MnO_{3-γ} (D = Ca, Sr) Manganites. *J. Exp. Theor. Phys.* **2003**, *96*, 1055–1064. <https://doi.org/10.1134/1.1591217>
57. Zubar, T. I.; Usovich, T. I.; Tishkevich, D. I.; Kanafyev, O. D.; Fedkin, V. A.; Kotelnikova, A. N.; Panasyuk, M. I.; Kurochka, A. S.; Nuriev, A. V.; Idris, A. M.; Khandaker, M. U.; Trukhanov, S. V.; Fedosyuk, V. M.; Trukhanov, A. V. Features of Galvanostatic Electrodeposition of NiFe Films with Composition Gradient: Influence of Substrate Characteristics. *Nanomaterials* **2022**, *12*, 2926. <https://doi.org/10.3390/nano12172926>
58. Trukhanov, S. V.; Troyanchuk, I. O.; Pushkarev, N. V.; Szymczak, H. Magnetic Properties of Anion-Deficient La_{1-x}Ba_xMnO_{3-x/2} (0 ≤ x ≤ 0.30) Manganites. *J. Exp. Theor. Phys.* **2003**, *96*, 110–117. <https://doi.org/10.1134/1.1545390>
59. Turchenko, V. A.; Trukhanov, S. V.; Kostishin, V. G.; Damay, F.; Porcher, F.; Klygach, D. S.; Vakhitov, M. G.; Matzui, L. Y.; Yakovenko, O. S.; Bozzo, B.; Fina, I.; Almessiere, M. A.; Slimani, Y.; Baykal, A.; Zhou, D.; Trukhanov, A. V. Impact of In³⁺ cations on structure and electromagnetic state of M-type hexaferrites. *J. Energy Chem.* **2022**, *69*, 667–679. <https://doi.org/10.1016/j.jechem.2021.12.027>
60. Izumi, F.; Momma, K. Three-Dimensional Visualization in Powder Diffraction. *Solid State Phenom.* **2007**, *130*, 15–20. <https://doi.org/10.4028/www.scientific.net/SSP.130.15>

TOC graphic

